

Article

A Through-the-Wall Imaging Approach Based on a TSVD/Variable-Exponent Lebesgue-Space Method

Andrea Randazzo ^{1,*} , Cristina Ponti ^{2,3} , Alessandro Fedeli ¹ , Claudio Estatico ⁴ , Paolo D'Atanasio ⁵,
Matteo Pastorino ¹ and Giuseppe Schettini ^{2,3}

- ¹ Department of Electrical, Electronic, Telecommunications Engineering and Naval Architecture, University of Genoa, 16145 Genoa, Italy; alessandro.fedeli@unige.it (A.F.); matteo.pastorino@unige.it (M.P.)
² Department of Engineering, Roma Tre University, 00146 Rome, Italy; cristina.ponti@uniroma3.it (C.P.); giuseppe.schettini@uniroma3.it (G.S.)
³ National Interuniversity Consortium for Telecommunications, Roma Tre University, 00146 Rome, Italy
⁴ Department of Mathematics, University of Genoa, 16146 Genoa, Italy; estatico@dima.unige.it
⁵ Italian National Agency for New Technologies, Energy and Sustainable Economic Development, Casaccia Research Center, 00123 Rome, Italy; paolo.datanasio@enea.it
* Correspondence: andrea.randazzo@unige.it

Abstract: A hybrid inversion scheme for through-the-wall imaging is proposed in this paper. The approach is based on a linearized model of the inverse-scattering problem, employing the Green's function developed for a layered background. The reconstruction is obtained by means of a Landweber-like iterative method performing a regularization in the framework of variable-exponent Lebesgue spaces. Thanks to the non-conventional geometrical properties of such spaces, it is possible to enhance the reconstruction capabilities, e.g., by promoting sparseness and reducing over-smoothing. The exponent function defining the specific space adopted in the inversion procedure is adaptively obtained directly from the measured data, through a truncated-singular value decomposition method. In this way, it is possible to precompute and reuse in both steps, for a given scenario, all the matrices necessary in the inversion process, thus leading to a computationally efficient solving strategy. The effectiveness of the approach is evaluated by using experimental data obtained with a commercial GPR apparatus employing a pulsed source field. A fast Fourier transform is applied to the time-domain measurements to extract frequency-domain data at a set of frequencies in the source spectrum, which are fed in input to the imaging scheme. Very good reconstruction capabilities are obtained both with a single metallic target, as well as in a challenging two targets layout including both a metallic object and a low-permittivity target.

Keywords: electromagnetic problems; through-wall radar; microwave imaging; inverse scattering



Citation: Randazzo, A.; Ponti, C.; Fedeli, A.; Estatico, C.; D'Atanasio, P.; Pastorino, M.; Schettini, G. A Through-the-Wall Imaging Approach Based on a TSVD/Variable-Exponent Lebesgue-Space Method. *Remote Sens.* **2021**, *13*, 2028. <https://doi.org/10.3390/rs13112028>

Academic Editor: Ali Khenchaf

Received: 12 April 2021

Accepted: 18 May 2021

Published: 21 May 2021

Publisher's Note: MDPI stays neutral with regard to jurisdictional claims in published maps and institutional affiliations.



Copyright: © 2021 by the authors. Licensee MDPI, Basel, Switzerland. This article is an open access article distributed under the terms and conditions of the Creative Commons Attribution (CC BY) license (<https://creativecommons.org/licenses/by/4.0/>).

1. Introduction

Through-the-wall imaging (TWI) is an application area that exploits penetration of microwave fields through building materials for the detection of humans or other targets hidden behind a wall, in a non-destructive way [1]. It addresses the needs of safety and surveillance in both civil and military operations. Due to the presence of a wall that separates the radar antennas and the target, the complexity of this imaging problem is enhanced compared to classical microwave imaging of free-space targets, or of targets buried in the subsoil, as in ground penetrating radar (GPR) applications [2]. Indeed, the scattering response may be strongly affected by the additional dielectric layer [3,4], since the electromagnetic signal undergoes significant effects of attenuation and distortion due to the multipath propagation occurring at the wall boundaries. The choice of the operational frequencies also plays an important role, and it is the result of a compromise: a better resolution can be achieved at higher frequencies, but at the expense of increased losses in the wall materials and lower penetration inside the building. These considerations

suggest the range 0.3–4 GHz as optimal in many TWI scenarios [5,6]. Different hardware architectures can be employed: a pulsed radar, where the source is radiating a wideband signal, or a frequency-stepped approach, where the source field is radiated in a limited number of frequencies.

The aims of TWI reconstruction may be different, according to the implemented approach. In most cases, the goal is the identification of the presence of the targets and the retrieval of their positions and shapes. This can be achieved, for example, through synthetic aperture radar approaches, that exploit beamforming techniques for the localization and imaging of static or moving targets [7–11]. Refocusing approaches to compensate image distortions due to multipath [12–14] and clutter by wall reflections [15–17] have been also considered. The concept of all-directions through-the-wall imaging with a large 2D synthetic aperture has been proposed in [18], and experimentally validated in [19]. Recently, the issue of mapping the internal walls of the building's interior has been considered to improve discrimination between walls and objects [20].

A different approach to TWI is given by inverse scattering algorithms. The developed algorithms mainly extend inverse scattering approaches of free space by including, in exact or approximate forms, the scattering effects introduced by the wall. In most cases, the scattering problem is tackled under a linearized form, e.g., using the Born or Kirchhoff approximations. This approach leads to a qualitative imaging, i.e., it returns target localization and a reconstruction of geometrical information, as target shape and detection of boundaries. Among the proposed techniques, widely used approaches are based on the truncated singular value decomposition (TSVD) [21–23], and linear sampling methods [24–26]. Moreover, in [27–29] the inverse scattering problems applied to TWI have been cast in the form of stochastic optimization approaches. Linearized TWI approaches can be also applied to the tracking of multiple moving targets, as in [30]. Strategies to suppress multipath ghosts, useful to improve targets detectability in a high-clutter environment, have been proposed in [31–33]. Compressive sensing (CS) has been explored, too, to enhance the reconstruction capabilities of targets in the presence of sparse scenarios [34–36]. In these implementations, small, mainly point-like, targets are assumed. Advanced CS formulations have also been proposed to solve the imaging problem in presence of ‘non sparse’ extended targets, as in [37,38]. CS applied to a multipath propagation scheme is proposed in [39], developed in a Bayesian framework. Although in some cases free-space Green's functions or other simplified formulations may be used in the reconstruction procedures, the adoption of a Green's function developed for a layered background provides a more accurate reconstruction by fully including the effects of the wall in the reconstruction algorithms [40–42]. A further approach is the quantitative imaging, i.e., the reconstruction of the distribution of the dielectric properties of the inspected scenario, which is obtained through fully non-linear inverse scattering techniques [43–46]. However, their practical implementation is quite challenging, also due to the wide investigation domains, and the limited-view data available from scanning. Finally, it is worth remarking that in many works, TWI algorithms are mainly validated against synthetic data, provided by numerical approaches. However, only validation against experimental data can assess reliability and limits of the reconstructions, while tackling the several non-idealities of real through-wall environments.

In this paper, a new TWI approach based on an inverse-scattering scheme developed in variable-exponent Lebesgue spaces is presented. In particular, the reconstruction is obtained by means of a hybrid procedure, where the TSVD is combined for the first time with a variable-exponent Landweber-like iterative method (VpLW). More in details, a preliminary image of the scenario is obtained by using the TSVD method, and it is used to build the exponent function of the variable-exponent Lebesgue spaces used in the subsequent Landweber-like scheme. In both steps, a linearized scattering model is adopted, which relies upon the use of the Green's function for a layered background for an accurate characterization of the multipath effects occurring at the wall boundaries.

In particular, the variable-exponent approach has been chosen since it has been found to provide significant enhancements in the reconstruction capabilities in different microwave imaging configurations [47,48]. Indeed, the exploitation of the geometrical properties of the variable-exponent Lebesgue spaces allows introducing non-standard regularization behaviors. For instance, it has been found that small values of the exponent function lead to a sparser reconstruction, which is beneficial for the background part of the imaging domain, whereas higher values (e.g., close to 2) improve the characterization of smooth profiles, such as those often shown by the targets. Moreover, the developed variable-exponent technique adaptively defines the values of the exponent function on the basis of a preliminary image, which in this work is obtained through a direct inversion of the adopted scattering operator by means of a TSVD-based approach.

It is worth remarking that this approach extends the one originally presented in [41], where however the exponent function was built using a delay-and-sum (DAS) beamforming technique. In that case, however, an approximate propagation model was adopted for characterizing the contribution of the wall, in which straight ray-propagation was assumed and the delays used in the beamforming process were obtained by solving, for every focusing point inside the investigation domain, an optimization problem for computing the shortest electric path from the transmitting–receiving antennas. The new approach has the advantage of allowing to use the same scattering model in both steps, which fully take into account the wall effects without approximations, while keeping the same good reconstruction capabilities of the original method. This also allows reusing the same underlying Green’s matrices, which can be thus precomputed for a given scenario, helping to increase the computational efficiency of the method.

Validation of the proposed TWI algorithm against experimental data is given. An experimental campaign is performed in a laboratory environment simulating a through-the-wall scenario, with a single wall hiding metallic or dielectric targets. A pulsed GPR is used in a fully bistatic mode for scanning the transmitting (TX) and receiving (RX) antenna locations under multi-view and multi-illumination mode. A set of measurements of the field scattered by the wall alone is preliminarily acquired in order to isolate the scattering response by the targets. Furthermore, the measured time-domain data have been pre-processed by using a Fourier transform to obtain the frequency-domain scattered-field data at the receiving antennas locations for a given set of frequencies, which are provided in input to the inversion procedure.

The paper is organized as follows. In Section 2, the proposed inverse scattering approach is reported. Application of the inversion procedure on experimental data is presented in Section 3. Conclusions follow in Section 4.

2. TWI Approach

In the considered imaging problem, one or more targets are located in an investigation area Ω behind a wall of thickness l_w and complex dielectric permittivity ϵ_w . Figure 1 shows a schematic diagram of the adopted configuration. In particular, in this figure, a horizontal cross-section of the scenario is shown, in which the wall is represented by the dark gray box. A two-dimensional configuration is assumed, where the dielectric properties of the targets and of the wall are constant along the z axis. The targets are illuminated by the electric field produced by a set of S antennas positioned in contact with the wall at positions \mathbf{r}_{ant}^s , $s = 1, \dots, S$ (indicated by the black triangles). In particular, a multi-view multi-illumination setup is considered, in which each antenna is used in turn in TX mode to generate the incident field, whereas the remaining $S - 1$ ones collect the total field produced by the interaction with the wall and the targets. Moreover, it is assumed that data at several working angular frequencies ω_f , $f = 1, \dots, F$, are available (an $e^{j\omega_f t}$ time-dependence is assumed and omitted from now on).

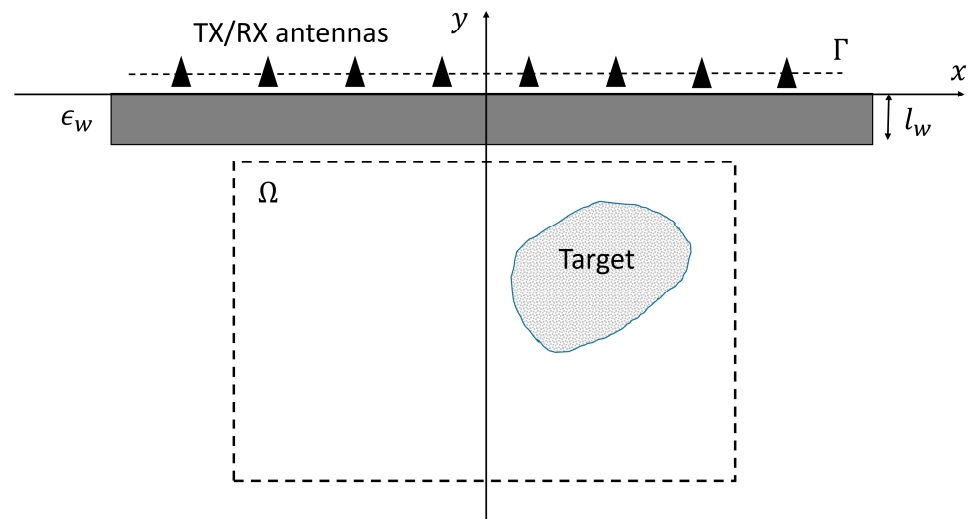


Figure 1. Through-the-wall imaging configuration.

In the following, the TX antennas are modeled as ideal line-current sources, i.e., they generate a transverse-magnetic (TM) electric field with z -component $\psi_{inc}^{s,f}(\mathbf{r}) = j\omega_f\mu_0 I^s G_{ml}(\mathbf{r}, \mathbf{r}_{ant}^s, \omega_f)$, where $\mathbf{r} = (x, y)$ is the position vector in the transverse plane, μ_0 is the magnetic permeability of vacuum, I^s is the current amplitude, and G_{ml} is the Green's function for the assumed three-layer configuration [49].

Under the previous assumptions, the z -component of the total field collected by the m -th antenna, $\psi_{tot}^{s,f}(\mathbf{r}_{ant}^m)$, can be expressed in terms of the dielectric properties of the investigation region through a non-linear scalar equation [2]. However, as often assumed in TWI settings, such a non-linear model can be simplified by using a first-order approximation, leading to the linear equation [22,50]

$$\psi_{sc}^{s,f}(\mathbf{r}_{ant}^m) = \int_{\Omega} \gamma(\mathbf{r}') G_{ml}(\mathbf{r}', \mathbf{r}_{ant}^s, \omega_f) G_{ml}(\mathbf{r}_{ant}^m, \mathbf{r}', \omega_f) d\mathbf{r}' \quad (1)$$

where $\psi_{sc}^{s,f}(\mathbf{r}_{ant}^m) = \psi_{tot}^{s,f}(\mathbf{r}_{ant}^m) - \psi_{inc}^{s,f}(\mathbf{r}_{ant}^m)$ is the z -component of the scattered electric field and γ is a function depending on the dielectric properties inside the investigation domain Ω . In particular, when weak scatterers are considered, γ is proportional to the contrast function, whereas if strong scatterers are present it assumes high values in correspondence to the targets, thus allowing to obtain an indication of their positions and shapes [22,50]. It is worth remarking that (1) relies upon the use of the Green's function G_{ml} for a three-layer medium (i.e., a dielectric slab is used to model the wall) [49], which allows including the wall effects directly in the scattering model. Moreover, $\psi_{sc}^{s,f}$ is obtained by subtracting from the total field (i.e., with the wall and the target) the contribution of the wall alone (i.e., the incident field $\psi_{inc}^{s,f}$). Consequently, γ contains only information about the targets behind the wall.

By discretizing the investigation domain into square subdomains Ω_n , $n = 1, \dots, N$, of side Δ in which γ is assumed constant, i.e., $\gamma_n = \gamma(\mathbf{r}_n)$, being \mathbf{r}_n the barycenter of the subdomain Ω_n , (1) can be written in discrete form as

$$\psi_{sc}^{s,f}(\mathbf{r}_{ant}^m) = \bar{g}(\mathbf{r}_{ant}^s, \mathbf{r}_{ant}^m, \omega_f) \cdot \bar{\gamma} \quad (2)$$

where $\bar{\gamma} = [\gamma_1, \dots, \gamma_N]^t$ and $\bar{g}(\mathbf{r}_{ant}^s, \mathbf{r}_{ant}^m, \omega_f)$ is an array of N elements whose n -th one is given by

$$\begin{aligned} g_n(\mathbf{r}_{ant}^s, \mathbf{r}_{ant}^m, \omega_f) &= \int_{\Omega_n} G_{ml}(\mathbf{r}', \mathbf{r}_{ant}^s, \omega_f) G_{ml}(\mathbf{r}_{ant}^m, \mathbf{r}', \omega_f) d\mathbf{r}' \\ &\cong G_{ml}(\mathbf{r}', \mathbf{r}_{ant}^s, \omega_f) G_{ml}(\mathbf{r}_{ant}^m, \mathbf{r}', \omega_f) \Delta^2 \end{aligned} \quad (3)$$

Finally, by stacking the equations related to the S illuminations, the $S - 1$ probing antennas, and the F working frequencies, the following discrete problem is attained

$$\bar{\psi}_{sc} = [G_{ml}] \bar{\gamma} \quad (4)$$

where $\bar{\psi}_{sc} = [\psi_{sc}^{1,1}(\mathbf{r}_{ant}^1), \dots, \psi_{sc}^{S,F}(\mathbf{r}_{ant}^{S-1})]^t$ is an array of length $FS(S - 1)$ containing all the available measurements and $[G_{ml}] = [\bar{g}(\mathbf{r}_{ant}^1, \mathbf{r}_{ant}^1, \omega_1), \dots, \bar{g}(\mathbf{r}_{ant}^S, \mathbf{r}_{ant}^{S-1}, \omega_F)]^t$ is a matrix of dimensions $FS(S - 1) \times N$ containing the values of the Green's function integrals in (3).

In order to obtain an image of the inspected scenario, (4) needs to be inverted for retrieving $\bar{\gamma}$. However, such an equation turns out to be severely ill-posed. Consequently, it is necessary to adopt proper regularization schemes. In this work, a hybrid approach is considered. In particular, it is based on a main loop performing a regularization in the framework of the Lebesgue spaces with variable exponent $L^{p(\cdot)}$ by means of truncated Landweber-like iterations [48]. To this end, it is assumed that the unknown space $\mathcal{U} = L^{p(\cdot)}(\mathbb{C}^N)$ and is equipped with a Luxemburg norm $\|\bar{\gamma}\|_{L^{p(\cdot)}}$ defined as [51]

$$\|\bar{\gamma}\|_{L^{p(\cdot)}} = \inf \left\{ \lambda > 0 : \sum_{n=1}^N \frac{1}{\lambda} |\gamma_n|^{p_n} \leq 1 \right\} \quad (5)$$

where $\bar{p} = [p_1, \dots, p_N]^t$ is an array containing the discretized exponent function. Moreover, a constant p -norm $\|\underline{\psi}\|_{L^{p_{av}}} = (\sum |\psi_n|^{p_{av}})^{1/p_{av}}$ is associated to the data space $\mathcal{D} = L^{p_{av}}(\mathbb{C}^{FS(S-1)})$, where the parameter p_{av} is set equal to the average of \bar{p} , i.e.,

$$p_{av} = \frac{1}{N} \sum_{n=1}^N p_n \quad (6)$$

In order to fully exploit the regularization capabilities of the variable-exponent regularization technique, it is necessary to define a proper exponent function. In particular, as discussed in the Introduction, low values are assigned to the regions belonging to the background, whereas higher ones to the points where a target is located. To this end, an initial image of the scenario, which allows an approximate localization of the targets, is built using a truncated singular value decomposition. The obtained image is then used to define the values of \bar{p} .

The developed VpLW-TSVD hybrid inversion method is summarized by the flow chart in Figure 2. In particular, the single steps are detailed as follows:

1. Initialization. The solution is initialized with a null vector, i.e., $\bar{\gamma}_0 = 0$ and the iteration index is set to $i = 0$;
2. TSVD initial reconstruction. An initial preliminary reconstruction is obtained by means of a truncated singular value decomposition as

$$\bar{\gamma}_{\text{TSVD}} = \sum_{i=1}^T \frac{\bar{v}_i^H \bar{\psi}_{sc}}{\sigma_i} \bar{u}_i \quad (7)$$

in which σ_i are the singular values of the matrix $[G_{ml}]$, \bar{u}_i and \bar{v}_i are the corresponding (left and right) singular vectors, and $T \leq \min(FS(S-1), N)$ is a suitable truncation index;

3. Exponent map construction. Using the initial TSVD reconstruction, the unknown-space exponent function (in discrete form) is computed as

$$\bar{p} = p_{min} + \Delta p \frac{\bar{\gamma}_{TSVD}}{\max_n \bar{\gamma}_{TSVD}} \quad (8)$$

where p_{min} and Δp are the prefixed minimum value and the range of the elements of \bar{p} , respectively. Moreover, the data-space exponent p_{av} is set equal to the average of \bar{p} according to (6);

4. Iterative update. The solution is iteratively updated as [47,48,52]:

$$\bar{\gamma}_{i+1} = \mathcal{J}_{\mathcal{U}}^* \left(\mathcal{J}_{\mathcal{U}}(\bar{\gamma}_i) - \beta [G_{ml}]^H \mathcal{J}_{\mathcal{D}}([G_{ml}]\bar{\gamma}_i - \bar{\psi}_{sc}) \right) \quad (9)$$

where $\mathcal{U}^* = L^{p^*(\cdot)}(\mathbb{C}^N)$ is the dual space of \mathcal{U} , with $p^*(\cdot) = p(\cdot)/(p(\cdot) - 1)$ the Hölder conjugate of $p(\cdot)$, $[G_{ml}]^H$ is the Hermitian transpose of $[G_{ml}]$, and β is a relaxation coefficient that is empirically computed as

$$\beta = 0.25 \left\{ \| [G_{ml}] \|_1^{-2} + (p_{av} - 1) \left(\| [G_{ml}] \|_2^{-2} - \| [G_{ml}] \|_1^{-2} \right) \right\} \quad (10)$$

In (9), $\mathcal{J}_{\mathcal{U}}$ and $\mathcal{J}_{\mathcal{D}}$ are the duality maps of the spaces $\mathcal{U} = L^{p(\cdot)}(\mathbb{C}^N)$ and $\mathcal{D} = L^{p_{av}}(\mathbb{C}^{FS(S-1)})$, respectively, which are defined as

$$\{ \mathcal{J}_{\mathcal{U}}(\bar{\gamma}) \}_n = \left(\sum_{k=1}^N \frac{p_k |\gamma_k|^{p_k}}{\| \bar{\gamma} \|_{L^{p(\cdot)}}^{p_k}} \right)^{-1} p_n |\gamma_n|^{p_n-1} \text{sign}(\gamma_n) \| \bar{\gamma} \|_{L^{p(\cdot)}}^{2-p_n}, \quad n = 1, \dots, N \quad (11)$$

$$\{ \mathcal{J}_{\mathcal{D}}(\bar{\psi}) \}_k = |\psi_k|^{p_{av}-1} \text{sign}(\psi_k) \| \bar{\psi} \|_{L^{p_{av}}}^{2-p_{av}}, \quad k = 1, \dots, FS(S-1) \quad (12)$$

where $\text{sign}(u) = u/|u|$ if $u \neq 0$ and zero otherwise;

5. Step 4 is iterated, with $i \leftarrow i + 1$, until a stopping criterion is fulfilled or a maximum number of iterations I_{max} is reached.

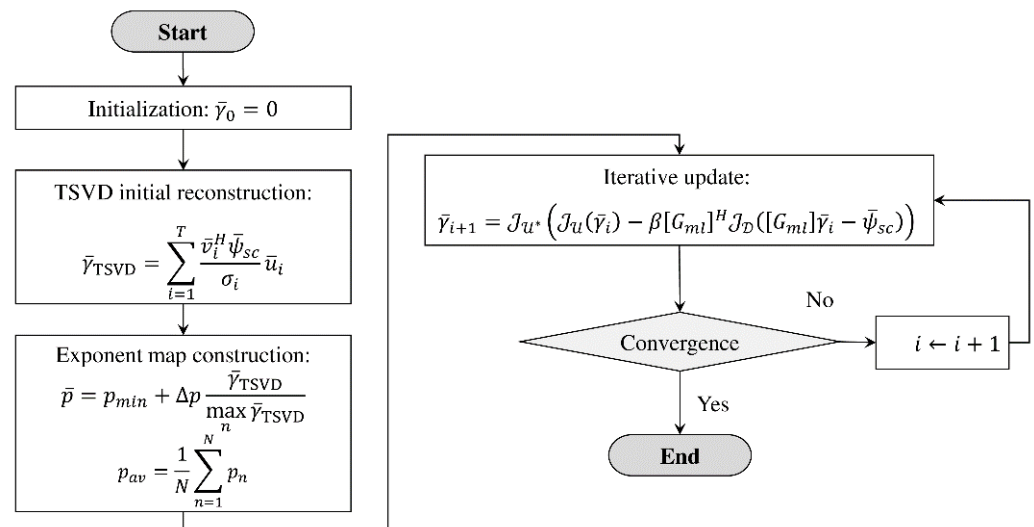


Figure 2. Block scheme of the developed TWI inversion procedure.

It is worth remarking that the developed approach aims at minimizing the following residual function

$$R_i = \frac{1}{2} \|\bar{\psi}_{sc} - [G_{ml}] \bar{\gamma}_i\|_{\mathcal{D}}^2 \quad (13)$$

However, differently from conventional methods, the update of the solution during the iterations is performed in the dual space \mathcal{U}^* of \mathcal{U} . In this way the method “moves” along non-standard directions, which are different from those of the anti-gradient used in standard inversion schemes in Hilbert spaces. This allows a better exploitation of the geometrical properties of the Banach spaces, by properly tuning the values of the exponent function [53]. In particular, when p is close to 1, a lower smoothing of the solution is obtained, thus improving the reconstruction of sparse regions with small and localized targets. On the other hand, higher regularization effects are obtained when p is higher, thus providing better reconstructions of parts with smooth dielectric variations.

3. Experimental Results

The algorithm described in Section 2 has been validated against experimental data collected in a laboratory environment. A commercial GPR, the PulseEKKO by Sensors and Software [54], has been employed to perform the experimental campaign. In particular, it has been used in a bistatic mode and mounts a transmitting antenna (TX) for radiating a broadband incident pulse with central frequency $f_c = 1$ GHz and a receiving antenna (RX) used for collecting the field produced by the scattering from the wall and the targets. Such an apparatus has been chosen thanks to its modularity. Indeed, since it permits the use of separate TX and RX antennas, it is possible to perform controllable multiple-input multiple-output measurements. Moreover, being a pulsed system, it allows collecting data over a significant bandwidth in the range usually adopted for TWI.

The TX and RX antennas are moved along a probing line of length L_S in order to synthesize a multi-view and multi-illumination setup. Specifically, they are sequentially located in the following $S = 16$ points along the wall:

$$x_{ant}^s = -\frac{L_S}{2} + sd, \quad s = 1, \dots, S \quad (14)$$

where $L_S = 2.175$ m and the distance between two adjacent positions is $d = 14.5$ cm.

The through-the-wall layout includes a brick wall of thickness 25 cm and estimated dielectric permittivity $\epsilon_w = 4.5\epsilon_0$ (the electric conductivity is negligible), hiding one or two targets given by: (a) one single metallic cylinder of circular cross-section of diameter 10 cm; (b) the metallic cylinder of case (a) and a wood cylinder of rectangular cross-section of sides 16 cm \times 8 cm in the same layout. Such targets represent two particularly significant cases for TWI applications. In the first configuration, a single target is assumed, with the aim of modeling highly reflective objects (e.g., metallic obstacles or human beings) that may be located behind the wall. In the second scenario, both a highly-reflecting object and a low scattering target are present at the same time. This is a particularly challenging case, since the scattering response from the highly-reflecting objects may mask the weak contributions from the low scattering ones.

In order to extract the scattered fields to be used as inputs for the inversion procedure, a set of measurements of the field scattered by the wall alone, i.e., without any target, has been preliminary collected and stored. Subsequently, they have been subtracted from the corresponding total field measured in the presence of the hidden objects before proceeding with the reconstruction. As a pulsed GPR is employed, a fast Fourier transform has been applied to the measured time-domain data for extracting the scattered-field data in a set of F different frequencies in the range [0.5, 2] GHz (i.e., inside the working bandwidth of the system).

In all the reported results, the investigation domain is a square area of side 1 m \times 1 m centered at a distance of 65 cm from the wall, which has been discretized into $N = 3969$ square subdomains of side $\Delta \cong 1.6$ cm. The minimum admissible value of the norm

exponent function has been set to 1.4, whereas the range is equal to $\Delta p = 0.6$. Such values have been selected on the basis of previous results available for free-space imaging using variable-exponent Lebesgue-space approaches. Indeed, it has been found that too low values of p_{min} may introduce instabilities, whereas higher values of Δp do not introduce significant enhancements. The maximum number of iterations is $I_{max} = 20$ and the iterations are stopped when the normalized difference of the data residual R_i between two adjacent iterations is below a fixed threshold $r_{th} = 0.01$, i.e., when $(R_{i-1} - R_i)/R_i \leq r_{th}$. The truncation index for the TSVD method has been computed by looking for the singular value below the threshold $\sigma_{th} = 0.4\sigma_0$ (σ_0 being the highest singular value). These values have been selected as a compromise to obtain good results in all the considered cases.

3.1. Single Metallic Target

Figure 3 shows a picture (Figure 3a) and a schematic diagram (Figure 3b) of the measurement setup. In this first target configuration, a single metallic object is located behind the wall (denoted by the black circle in Figure 3b). In particular, a circular cylinder of diameter $D = 10$ cm has been positioned at a distance of $h_c = 50$ cm from the wall, with an offset of 19 cm from the center of the probing line.

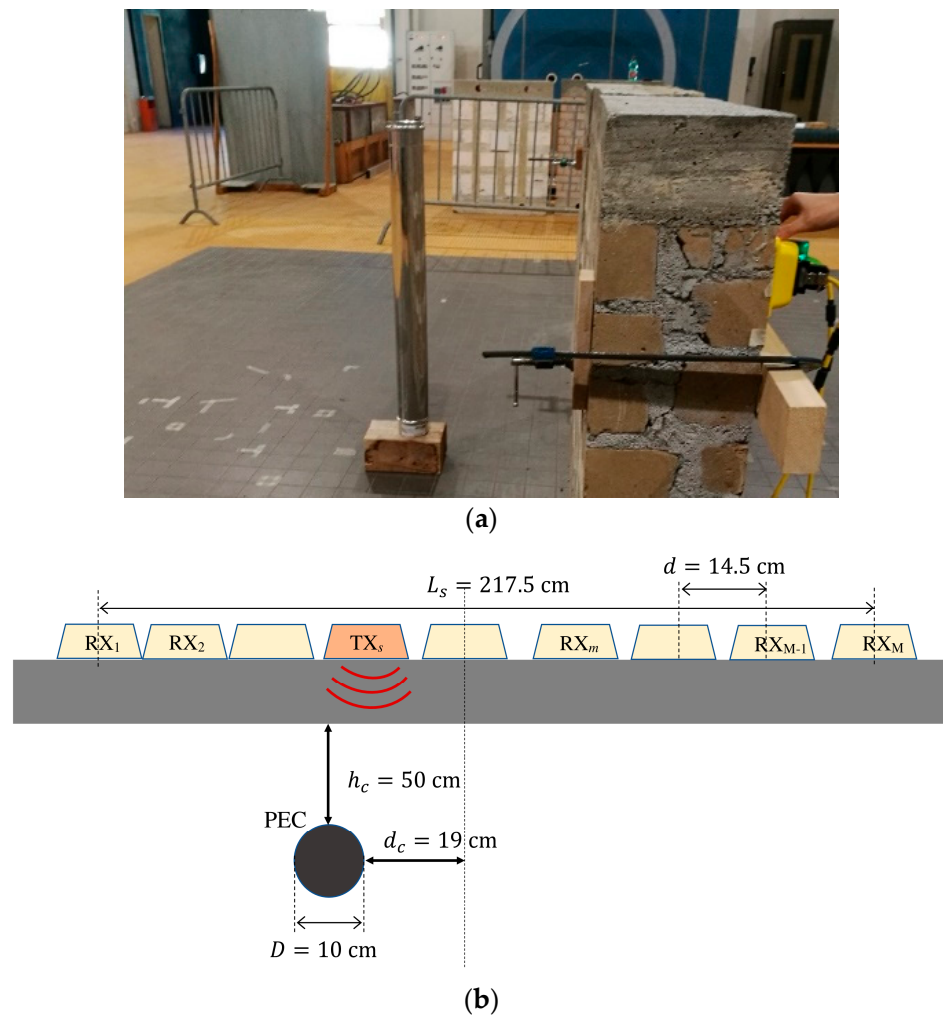


Figure 3. (a) Picture and (b) schematic representation of the first target scenario. Single off-centered metallic cylinder.

Such a target has been chosen since the high reflectivity of the metallic cylinder may be representative of very high-scattering objects that may be present in the scenario (e.g., metallic poles), as well as, although in an approximate way as often done in the TWI

literature, of a human target, due to its significant dielectric contrast with respect to the background medium. The arrangement of the TX (yellow boxes) and RX (orange box) antennas is also schematically shown in Figure 3b for the generic s -th view. In order to evaluate the effect of the number of frequencies used in the inversion procedure, the number F of frequency samples extracted from the Fourier transform has been varied between 3 and 41. The frequency range has been kept constant and equal to [0.3, 2] GHz.

Figure 4a–c show the behavior of the estimated coordinates of the target center and its diameter extracted from the reconstructed images versus the number of frequencies. Such values are found by setting a threshold of $1/3$ on the normalized reconstructed distribution of $\bar{\gamma}$ and by searching for the minimum circle enclosing the pixels over such a value in a square region of side 30 cm around the actual target location. In particular, both the results obtained by considering the hybrid approach and the TSVD method alone are reported. As can be seen, in almost all cases, the position of the target is correctly estimated. However, the dimension found using the TSVD method alone is always overestimated. Moreover, the hybrid method allows obtaining good results even when using a significantly lower number of frequencies (i.e., higher than 5). Finally, the signal-to-clutter ratio (SCR) of the retrieved images of the inspected scenario, defined as [55]

$$SCR = 20 \log_{10} \left(N_b \frac{\max_{n \in target} |\gamma_n|}{\sum_{n \in background} |\gamma_n|} \right) \quad (15)$$

has also been computed and shown in Figure 4d.

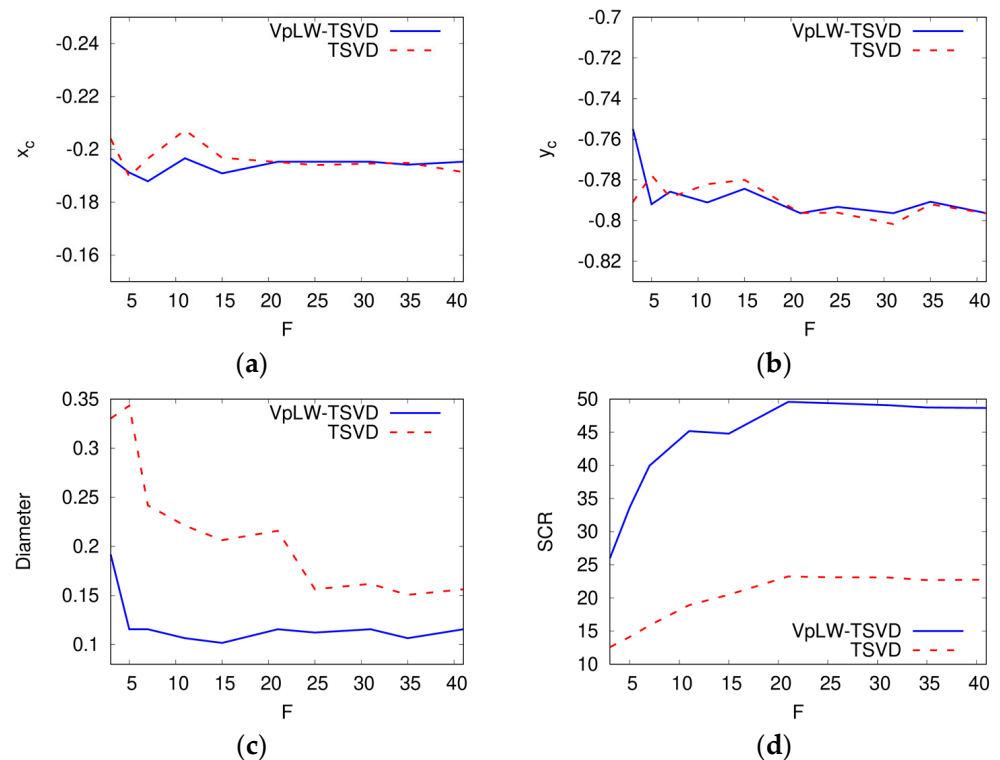


Figure 4. Reconstructed (a,b) position and (c) diameter of the cylinder versus the number of processed frequencies. (d) Signal-to-clutter ratio of the corresponding retrieved images. Single off-centered metallic cylinder.

As can be seen, the proposed hybrid approach allows obtaining images significantly cleaner than those of the TSVD method alone (the difference between the SCR for the two approaches is almost always higher than 20 dB). Moreover, this graph suggests that a

number of frequencies greater than about 20 is sufficient to achieve the best reconstruction quality, since increasing F does not result in a higher SCR.

Such results are also confirmed by the normalized images of the retrieved distribution of $\bar{\gamma}$, i.e., $I^N = \bar{\gamma}/\max|\bar{\gamma}|$, shown in Figure 5. Indeed, when only $F = 7$ frequencies are considered, the TSVD image is characterized by significant artifacts and the dimension of the object is slightly overestimated (especially in the vertical direction). Nevertheless, the hybrid approach is able to provide a quite good reconstruction, almost free of artifacts. Increasing the number of frequencies (as in Figure 5c,d, where $F = 25$) leads to a better initial estimation with the TSVD method, which in turn results in a clean final image, where the target can be clearly identified and whose dimensions are correctly estimated.

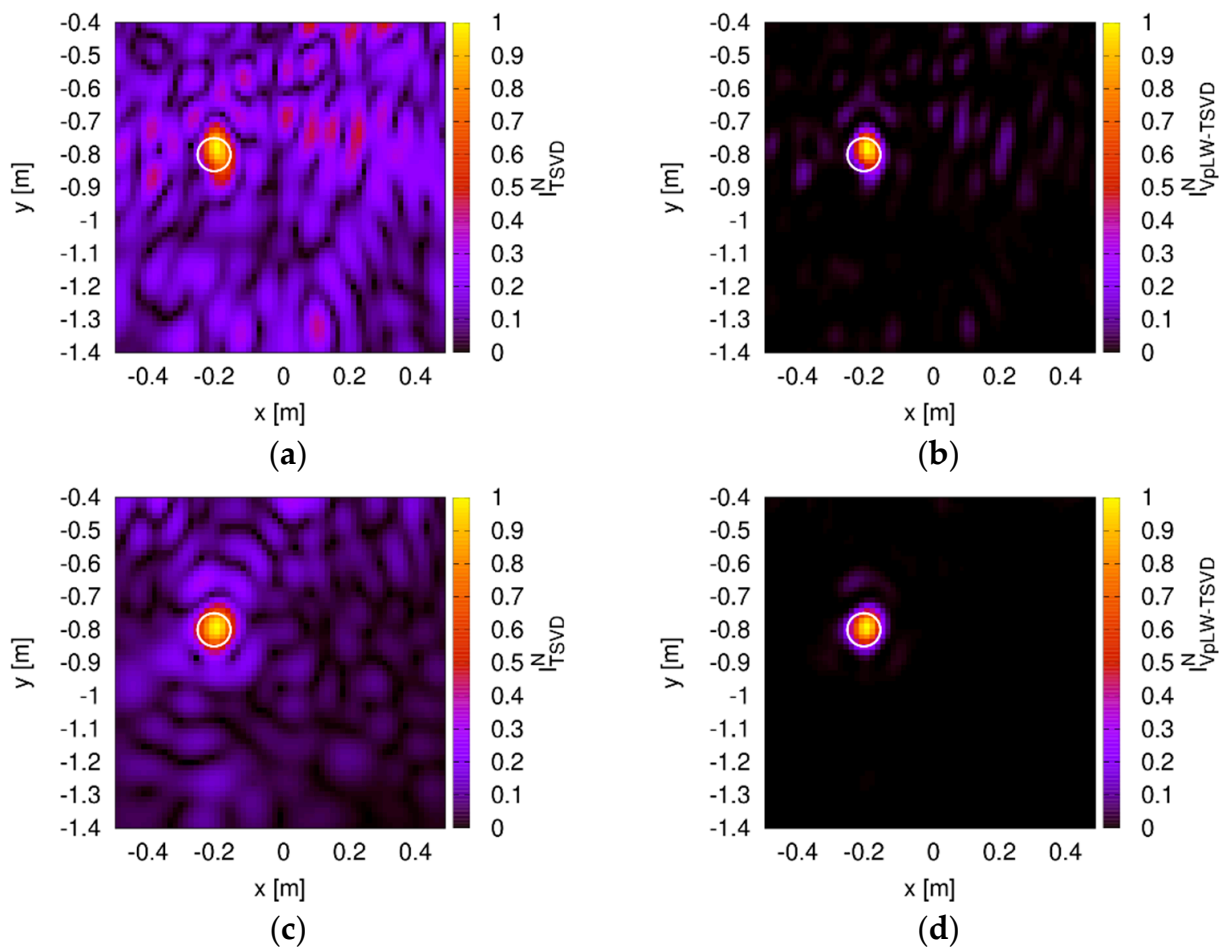


Figure 5. Normalized reconstructed images. (a) TSVD and (b) hybrid variable-exponent approaches, $F = 7$ frequency samples. (c) TSVD and (d) hybrid variable-exponent approaches, $F = 25$ frequency samples. Single off-centered metallic cylinder.

Finally, the effects on the reconstruction capabilities of the number of subdomains used to discretize the investigation area, and consequently of the size Δ of each pixel of the image, have been evaluated in the case $F = 25$. In particular, N has been varied between 400 and 10,000 (corresponding to $\Delta \in [0.01, 0.05]$ m). The obtained results, which are summarized in Table 1, show that the developed approach is quite stable with respect to such a parameter. Indeed, the diameter is almost always estimated correctly. A similar behavior is also shown by the estimated center (not reported for sake of brevity). Moreover, the SCR slightly increases with N .

Table 1. Estimated diameter, SCR, and computational times versus the number of subdomains used to discretize the inspected region. Single off-centered metallic cylinder, $F = 25$ frequency samples.

N	Δ [cm]	D [cm]	SCR [dB]	Offline Time [s]		Online Time [s]	
				$[G_{ml}]$ Precomputation	$(\sigma_i, \bar{u}_i, \bar{v}_i)$ Precomputation	SVD Inversion	VpLW Inversion
400	5	7.1	42.0	23.7	17.1	2.1×10^{-3}	0.3
1600	2.5	10.3	46.0	139.2	34.1	3.9×10^{-3}	0.75
3600	1.67	10.5	49.7	281.9	123.7	2×10^{-3}	0.86
6400	1.25	10.8	50.6	524.0	280.9	3×10^{-3}	1.28
10,000	1	10.8	51.5	761.3	549.9	3×10^{-3}	1.37

Such considerations are also confirmed by the examples of reconstructed images shown in Figure 6. When N is low (e.g., $N = 400$), the pixels are large and, thus, do not allow an exact shaping of the target, although its position and dimensions are close to the actual ones. Moreover, an artifact is present above the target. When N is increased, the reconstruction quality improves, allowing a better identification of the shape of the target.

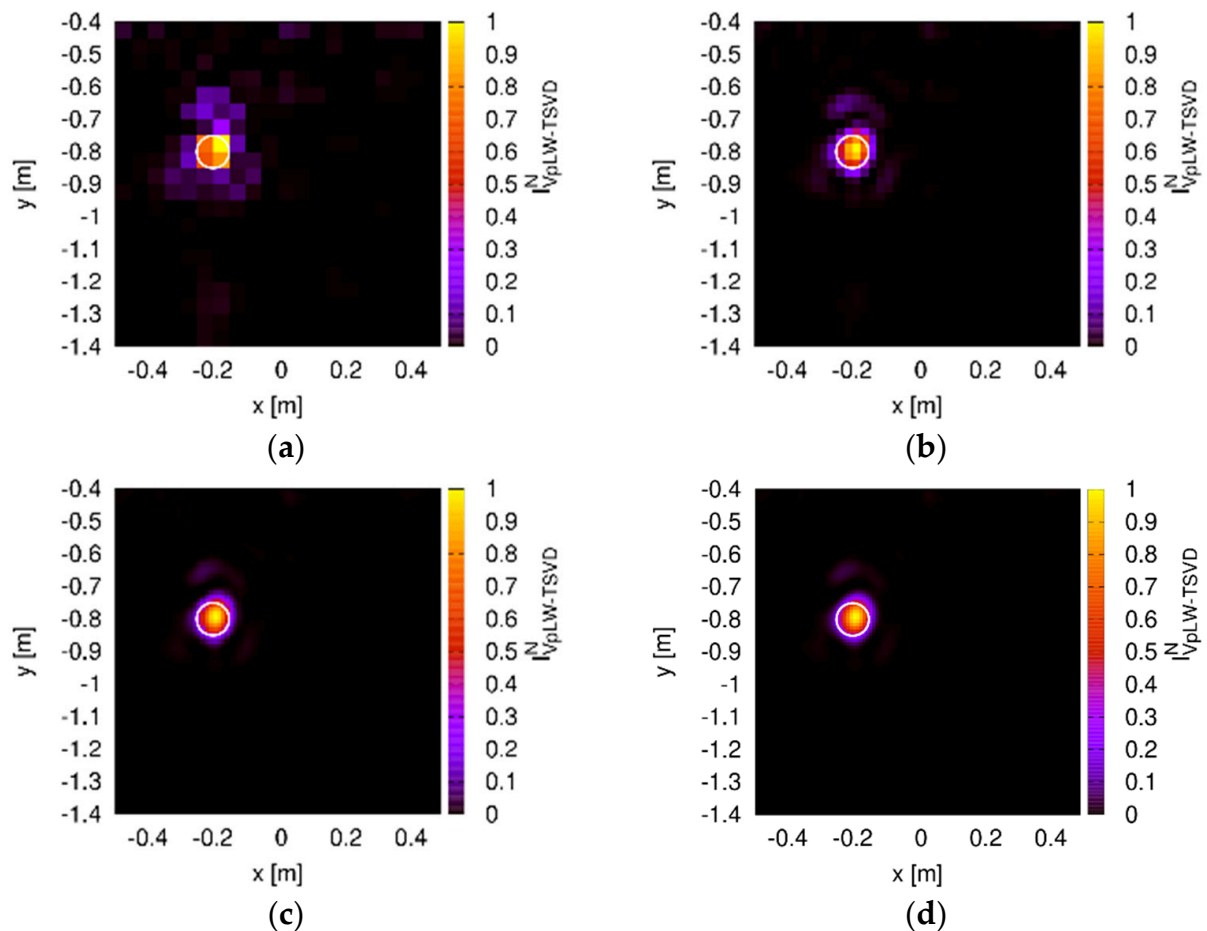


Figure 6. Normalized reconstructed images for different numbers of subdomains used to discretize the inspected region. (a) $N = 400$, (b) $N = 1600$, (c) $N = 6400$, (d) $N = 10,000$. Single off-centered metallic cylinder, $F = 25$ frequency samples.

For completeness, Table 1 also reports the computational times required for running the inversion code on a standard laptop PC equipped with an Intel Core i5-8265U @ 1.60 GHz CPU with 16 GB of RAM. It is worth remarking that, once the scenario is defined, the matrix $[G_{ml}]$ and its singular value decomposition can be computed once for all and offline. Consequently, in the table, the time dedicated to such a precomputing step has been

separated from the online time necessary to actually perform the inversion. Moreover, since the TSVD and VpLW steps of the inversion procedure rely upon the use of the same matrix $[G_{ml}]$, it can be computed just one time and reused in both stages, allowing an increase in the computational efficiency of the method. Such a consideration is confirmed by the online times shown in Table 1. Indeed, since all the necessary quantities are precomputed, the TSVD inversion in (7) requires a negligible time, whereas the VpLW step requires approximately 1 s.

3.2. Metallic and Dielectric Targets

As a second configuration, a more challenging scenario, in which two separate targets are located behind the wall, has been considered. Figure 7 shows a picture and a schematic representation of the considered scenario. In particular, the first target is the same metallic cylinder considered in the previous section (i.e., with diameter $D = 10$ cm and at distance of $h_c = 50$ cm from the wall) but with an increased offset $d_c = 35$ cm from the center of the probing line. The second object (schematized by the brown rectangle in Figure 7b) is a low scattering rectangular cylinder made of wood with sides $a = 16$ cm and $b = 8$ cm, which is located at a distance $h_w = 40$ cm from the wall with an offset $d_w = 22$ cm from the center.

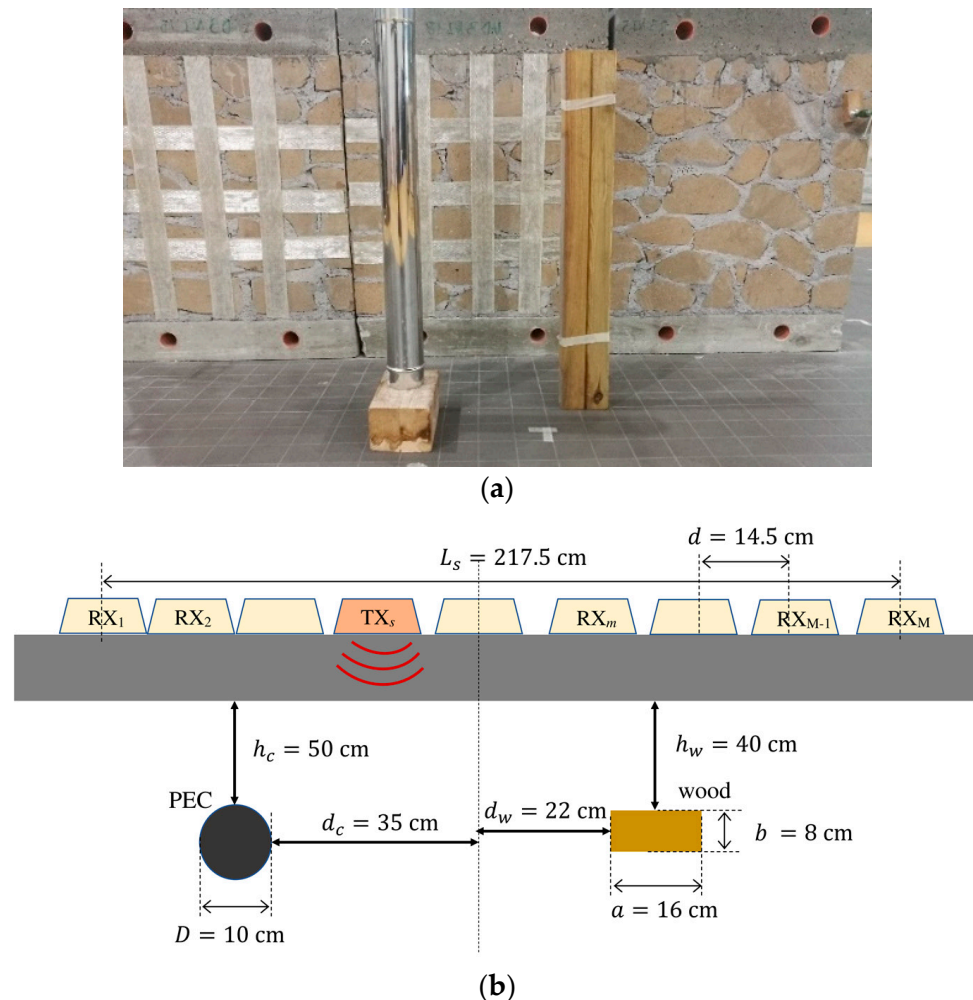


Figure 7. (a) Picture and (b) schematic representation of the second target scenario. Separate metallic and wood cylinders.

The choice of the wood cylinder, with its low dielectric permittivity, allows checking the effectiveness of the technique in the detection of weak scatterers, especially when interacting with stronger scatterers, as in the considered layout. This is representative of

practical challenging TW environments, where the target of the survey must be discriminated from other scatterers and pieces of furniture. The arrangement of the antennas is the same as in the previous case, as schematized in Figure 7b.

The retrieved normalized distribution of $\bar{\gamma}$ is shown in Figure 8. In particular, Figure 8a reports the results obtained by the TSVD method alone, whereas the final reconstruction provided by the hybrid method is given in Figure 8b. As can be seen, the initial TSVD image already allows identifying the metallic cylinder. However, significant artifacts are present in the background. Moreover, the wood object cannot be readily seen, since the amplitude of its contribution is comparable to the background noise. However, the application of the hybrid technique greatly enhances the quality of the final image. Indeed, the background is completely free from artifacts, the metallic cylinder is correctly localized and sized, and the low-scattering wood object can be distinguished, although with a lower amplitude.

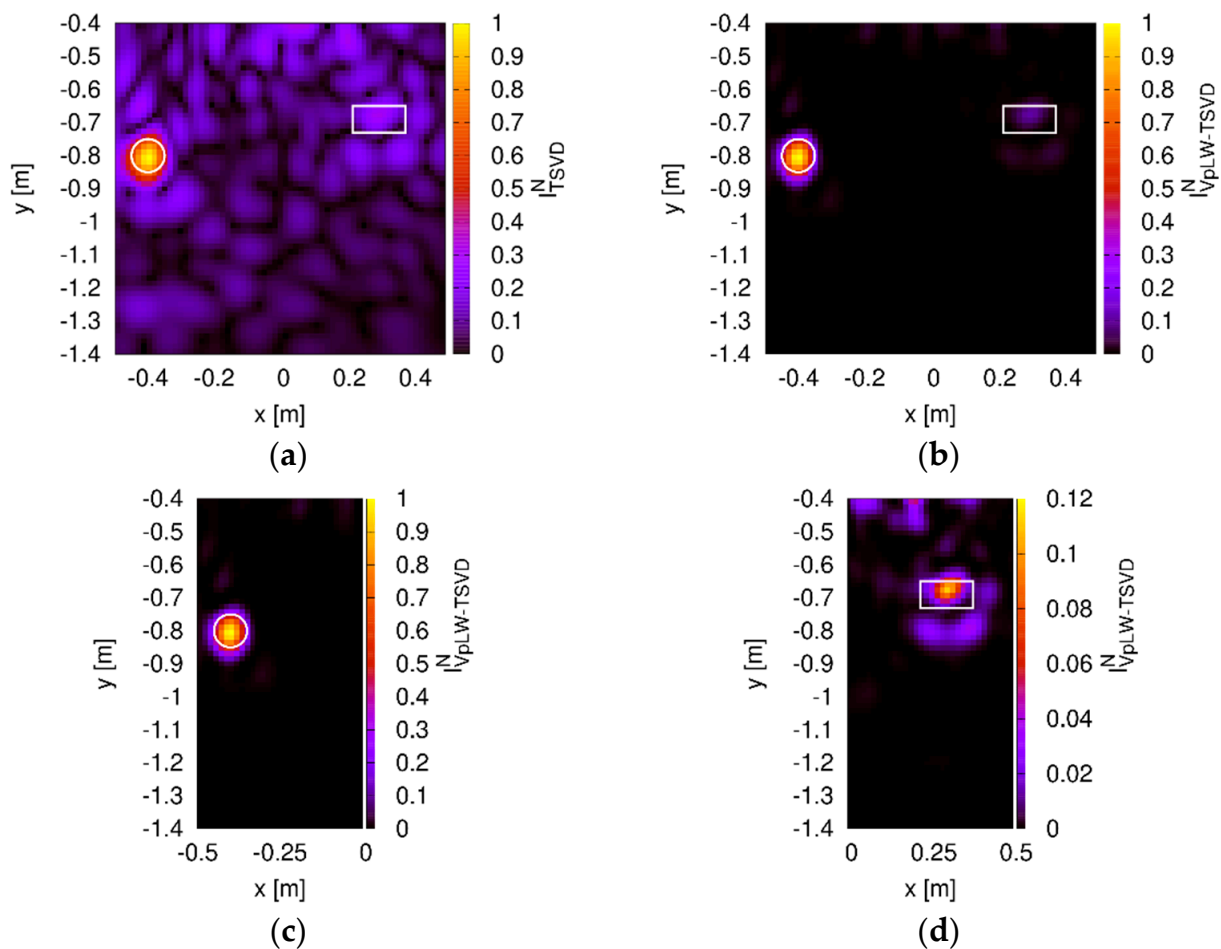


Figure 8. Normalized reconstructed images. (a) TSVD and (b) hybrid variable-exponent approaches, $F = 25$ frequency samples. Zooms on the (c) left and (d) right parts of the investigation domain. Separate metallic and wood cylinders.

This fact is confirmed by the values of the SCR: for the TSVD alone it is equal to 22, whereas when considering the hybrid approach it increases to 46.3. In order to better analyze this last result, zooms on the left and right parts of the image are provided in Figure 8c,d (with the color scale adapted to the respective maximum amplitudes). Now the wood target can be clearly identified in Figure 8c, and its amplitude is significantly higher than the small artifacts that can be seen in the image.

The results obtained by conventional DAS beamforming techniques [7,56–58] are also shown in Figure 9 for comparison purposes. In particular, two cases have been considered. In the first one (Figure 9a), a standard free-space approach, in which the effects of the wall are neglected, is adopted. As expected, the resulting image is totally unfocused and the

targets cannot be even identified. Things get better if the wall is properly compensated (Figure 9b). In this case, the delays used in the beamforming process are computed by taking into account the propagation through the wall by exploiting the Fermat's principle. As can be seen, the beamforming results are now similar to the ones provided by the TSVD approach alone, although the weaker target has a lower amplitude and the dimension of the PEC cylinder is larger. However, it should be noted that now a different (and approximate) propagation model is used: this does not allow reusing the same matrix already computed for the VpLW method. In particular, for every focusing point, it is necessary to solve a time-consuming optimization problem to find the shortest electrical path of the Fermat's principle.

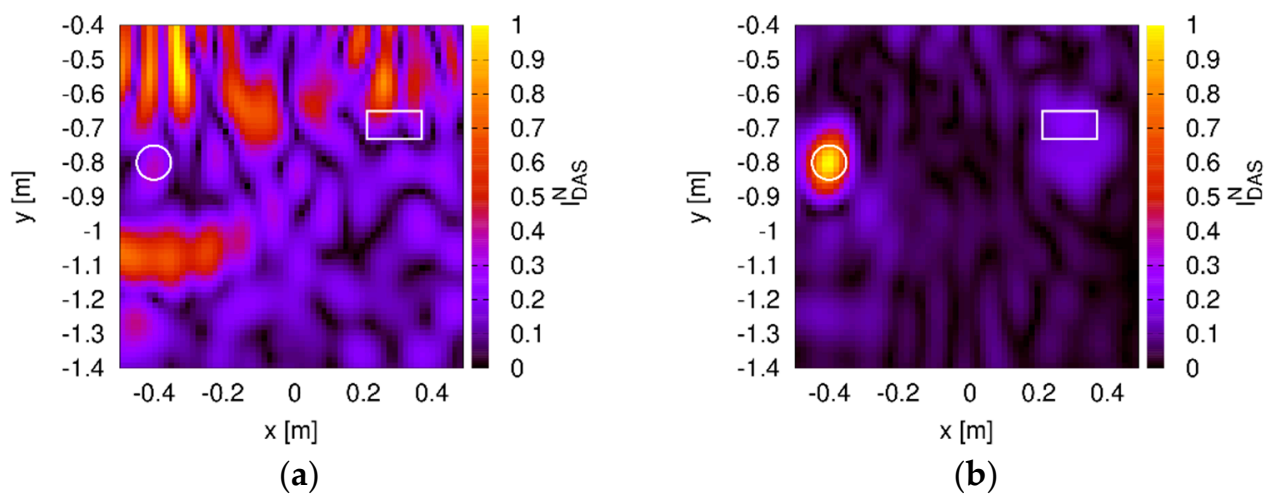


Figure 9. Normalized reconstructed images obtained with conventional DAS beamforming (a) without and (b) with wall compensation. Separate metallic and wood cylinders.

4. Conclusions

In this paper, a novel inverse-scattering-based approach for through-the-wall imaging has been presented. The developed approach relies upon the use of a linearized scattering model, in which a Green's function for stratified media is adopted for fully taking into account the scattering effects of the wall. The obtained inverse problem is solved, in a regularized sense, by means of an iterative scheme developed in the context of the variable-exponent Lebesgue spaces. The function defining the exponent of the spaces used in the inversion is built directly from the available measurements by using a truncated singular value decomposition approach. This first step uses the same Green's matrices necessary for the subsequent inversion, which can be then precomputed in order to increase the computational efficiency of the method. The performance of the developed inversion technique has been evaluated by means of experimental measurements performed in a laboratory and considering different targets. The obtained results confirm that the approach allows an accurate reconstruction of the inspected scenario, providing better results, especially in terms of clutter rejection, than the TSVD method alone. Future works will be aimed at the extension of the procedure to full three-dimensional imaging, to the introduction of proper terms for compensating the antenna behavior, and the development of non-linear techniques providing a complete reconstruction of the distributions of dielectric properties of the targets.

Author Contributions: Conceptualization, A.R., C.P., A.F., C.E., M.P. and G.S.; formal analysis A.R., C.P., A.F., C.E., M.P. and G.S.; methodology A.R., C.P., A.F., C.E., M.P. and G.S.; validation, A.R., C.P., A.F., C.E., P.D., M.P. and G.S. All authors have read and agreed to the published version of the manuscript.

Funding: This research was partially supported by the Italian Ministry for Education, University, and Research under the project PRIN2015 U-VIEW, grant number 20152HWRSL.

Data Availability Statement: The data used in this study are not publicly available.

Conflicts of Interest: The authors declare no conflict of interest.

References

1. Amin, M.G. (Ed.) *Through-the-Wall Radar Imaging*; CRC Press: Boca Raton, FL, USA, 2011.
2. Pastorino, M.; Randazzo, A. *Microwave Imaging Methods and Applications*; Artech House: Boston, MA, USA, 2018.
3. Valagiannopoulos, C.A.; Tsitsas, N.L.; Sihvola, A.H. Unlocking the ground: Increasing the detectability of buried objects by depositing passive superstrates. *IEEE Trans. Geosci. Remote Sens.* **2016**, *54*, 3697–3706. [\[CrossRef\]](#)
4. Valagiannopoulos, C.A.; Tsitsas, N.L.; Sihvola, A.H. Hiding a bump on a PEC plane by using an isotropic lossless dielectric layer. *IEEE Trans. Antennas Propag.* **2014**, *62*, 5706–5714. [\[CrossRef\]](#)
5. Nkwari, P.K.M.; Sinha, S.; Ferreira, H.C. Through-the-wall radar imaging: A review. *IETE Tech. Rev.* **2018**, *35*, 631–639. [\[CrossRef\]](#)
6. Cicchetti, R.; Cicchetti, V.; Faraone, A.; Foged, L.; Testa, O. A compact high-gain wideband lens vivaldi antenna for wireless communications and through-the-wall imaging. *IEEE Trans. Antennas Propag.* **2020**. [\[CrossRef\]](#)
7. Ahmad, F.; Amin, M.G.; Kassam, S.A. Synthetic aperture beamformer for imaging through a dielectric wall. *IEEE Trans. Aerosp. Electron. Syst.* **2005**, *41*, 271–283. [\[CrossRef\]](#)
8. Zhang, W.; Hoorfar, A. Three-dimensional synthetic aperture radar imaging through multilayered walls. *IEEE Trans. Antennas Propag.* **2014**, *62*, 459–462. [\[CrossRef\]](#)
9. Cicchetti, R.; Pisa, S.; Piuze, E.; Pittella, E.; D’Atanasio, P.; Testa, O. Numerical and experimental comparison among a new hybrid FT-MUSIC technique and existing algorithms for through-the-wall radar imaging. *IEEE Trans. Microw. Theory Tech.* **2021**. [\[CrossRef\]](#)
10. Dehmollaian, M.; Thiel, M.; Sarabandi, K. Through-the-wall imaging using differential SAR. *IEEE Trans. Geosci. Remote Sens.* **2009**, *47*, 5. [\[CrossRef\]](#)
11. Klibanov, M.V.; Smirnov, A.V.; Khoa, V.A.; Sullivan, A.J.; Nguyen, L.H. Through-the-wall nonlinear SAR imaging. *IEEE Trans. Geosci. Remote Sens.* **2021**, 1–12. [\[CrossRef\]](#)
12. Dehmollaian, M.; Sarabandi, K. Refocusing through building walls using synthetic aperture radar. *IEEE Trans. Geosci. Remote Sens.* **2008**, *46*, 6. [\[CrossRef\]](#)
13. Setlur, P.; Amin, M.; Ahmad, F. Multipath model and exploitation in through-the-wall and urban radar sensing. *IEEE Trans. Geosci. Remote Sens.* **2011**, *49*, 10. [\[CrossRef\]](#)
14. Xin, S.; Biying, L.; Pengfei, L.; Zhimin, Z. A multiarray refocusing approach for through-the-wall imaging. *IEEE Geosci. Remote Sens. Lett.* **2015**, *12*, 4. [\[CrossRef\]](#)
15. Liu, H.; Huang, C.; Gan, L.; Zhou, Y.; Truong, T.-K. Clutter reduction and target tracking in through-the-wall radar. *IEEE Trans. Geosci. Remote Sens.* **2020**, *58*, 1. [\[CrossRef\]](#)
16. Tivive, F.H.C.; Bouzerdoum, A.; Amin, M.G. A subspace projection approach for wall clutter mitigation in through-the-wall radar imaging. *IEEE Trans. Geosci. Remote Sens.* **2015**, *53*, 2108–2122. [\[CrossRef\]](#)
17. Zhou, Y.; Huang, C.; Liu, H.; Li, D.; Truong, T.-K. Front-wall clutter removal in through-the-wall radar based on weighted nuclear norm minimization. *IEEE Geosci. Remote Sens. Lett.* **2020**, 1–5. [\[CrossRef\]](#)
18. Yektakhah, B.; Sarabandi, K. All-directions through-the-wall radar imaging using a small number of moving transceivers. *IEEE Trans. Geosci. Remote Sens.* **2016**, *54*, 11. [\[CrossRef\]](#)
19. Yektakhah, B.; Sarabandi, K. All-directions through-the-wall imaging using a small number of moving omnidirectional bi-static FMCW transceivers. *IEEE Trans. Geosci. Remote Sens.* **2019**, *57*, 2618–2627. [\[CrossRef\]](#)
20. Yektakhah, B.; Sarabandi, K. A method for detection of flat walls in through-the-wall SAR imaging. *IEEE Geosci. Remote Sens. Lett.* **2020**, 1–5. [\[CrossRef\]](#)
21. Soldovieri, F.; Solimene, R. Through-wall imaging via a linear inverse scattering algorithm. *IEEE Geosci. Remote Sens. Lett.* **2007**, *4*, 4. [\[CrossRef\]](#)
22. Solimene, R.; Soldovieri, F.; Prisco, G.; Pierri, R. Three-dimensional through-wall imaging under ambiguous wall parameters. *IEEE Trans. Geosci. Remote Sens.* **2009**, *47*, 5. [\[CrossRef\]](#)
23. Soldovieri, F.; Solimene, R.; Brancaccio, A.; Pierri, R. Localization of the interfaces of a slab hidden behind a wall. *IEEE Trans. Geosci. Remote Sens.* **2007**, *45*, 8. [\[CrossRef\]](#)
24. Charnley, M.; Wood, A. A linear sampling method for through-the-wall radar detection. *J. Comput. Phys.* **2017**, *347*, 147–159. [\[CrossRef\]](#)

25. Catapano, I.; Crocco, L. A qualitative inverse scattering method for through-the-wall imaging. *IEEE Geosci. Remote Sens. Lett.* **2010**, *7*, 685–689. [\[CrossRef\]](#)
26. Gennarelli, G.; Vivone, G.; Braca, P.; Soldovieri, F.; Amin, M.G. Comparative analysis of two approaches for multipath ghost suppression in radar imaging. *IEEE Geosci. Remote Sens. Lett.* **2016**, *13*, 9. [\[CrossRef\]](#)
27. Chiu, C.-C.; Sun, C.-H. Through-wall imaging for a metallic cylinder. *Nondestruct. Test. Eval.* **2013**, *28*, 72–81. [\[CrossRef\]](#)
28. Dehmollaian, M. Through-wall shape reconstruction and wall parameters estimation using differential evolution. *IEEE Geosci. Remote Sens. Lett.* **2011**, *8*, 201–205. [\[CrossRef\]](#)
29. Rekanos, I.T. Shape reconstruction of a perfectly conducting scatterer using differential evolution and particle swarm optimization. *IEEE Trans. Geosci. Remote Sens.* **2008**, *46*, 1967–1974. [\[CrossRef\]](#)
30. Gennarelli, G.; Vivone, G.; Braca, P.; Soldovieri, F.; Amin, M.G. Multiple extended target tracking for through-wall radars. *IEEE Trans. Geosci. Remote Sens.* **2015**, *53*, 12. [\[CrossRef\]](#)
31. Liu, J.; Kong, L.; Yang, X.; Liu, Q.H. First-order multipath ghosts' characteristics and suppression in MIMO through-wall imaging. *IEEE Geosci. Remote Sens. Lett.* **2016**, *13*, 1315–1319. [\[CrossRef\]](#)
32. Guo, S.; Yang, X.; Cui, G.; Song, Y.; Kong, L. Multipath ghost suppression for through-the-wall imaging radar via array rotating. *IEEE Geosci. Remote Sens. Lett.* **2018**, *15*, 868–872. [\[CrossRef\]](#)
33. Tan, Q.; Leung, H.; Song, Y.; Wang, T. Multipath ghost suppression for through-the-wall radar. *IEEE Trans. Aerosp. Electron. Syst.* **2014**, *50*, 2284–2292. [\[CrossRef\]](#)
34. Wu, Q.; Zhang, Y.D.; Ahmad, F.; Amin, M.G. Compressive-sensing-based high-resolution polarimetric through-the-wall radar imaging exploiting target characteristics. *Antennas Wirel. Propag. Lett.* **2015**, *14*, 1043–1047. [\[CrossRef\]](#)
35. Huang, Q.; Qu, L.; Wu, B.; Fang, G. UWB through-wall imaging based on compressive sensing. *IEEE Trans. Geosci. Remote Sens.* **2010**, *48*, 1408–1415. [\[CrossRef\]](#)
36. Solimene, R.; Ahmad, F.; Soldovieri, F. A novel CS-TSVD strategy to perform data reduction in linear inverse scattering problems. *IEEE Geosci. Remote Sens. Lett.* **2012**, *9*, 881–885. [\[CrossRef\]](#)
37. Oliveri, G.; Anselmi, N.; Massa, A. Compressive sensing imaging of non-sparse 2D scatterers by a total-variation approach within the Born approximation. *IEEE Trans. Antennas Propag.* **2014**, *62*, 5157–5170. [\[CrossRef\]](#)
38. Tang, V.H.; Bouzerdoun, A.; Phung, S.L. Compressive radar imaging of stationary indoor targets with low-rank plus jointly sparse and total variation regularizations. *IEEE Trans. Image Process.* **2020**, *29*, 4598–4613. [\[CrossRef\]](#) [\[PubMed\]](#)
39. Wu, Q.; Lai, Z.; Amin, M.G. Through-the-wall radar imaging based on Bayesian compressive sensing exploiting multipath and target structure. *IEEE Trans. Comput. Imaging* **2021**, *7*, 422–435. [\[CrossRef\]](#)
40. Fedeli, A.; Pastorino, M.; Ponti, C.; Randazzo, A.; Schettini, G. Through-the-wall microwave imaging: Forward and inverse scattering modeling. *Sensors* **2020**, *20*, 2865. [\[CrossRef\]](#) [\[PubMed\]](#)
41. Randazzo, A.; Ponti, C.; Fedeli, A.; Estatico, C.; D'Atanasio, P.; Pastorino, M.; Schettini, G. A two-step inverse-scattering technique in variable-exponent Lebesgue spaces for through-the-wall microwave imaging: Experimental results. *IEEE Trans. Geosci. Remote Sens.* **2021**. [\[CrossRef\]](#)
42. Zhang, W.; Hoorfar, A. Three-dimensional real-time through-the-wall radar imaging with diffraction tomographic algorithm. *IEEE Trans. Geosci. Remote Sens.* **2013**, *51*, 4155–4163. [\[CrossRef\]](#)
43. Chu, Y.; Xu, K.; Zhong, Y.; Ye, X.; Zhou, T.; Chen, X.; Wang, G. Fast microwave through wall imaging method with inhomogeneous background based on levenberg–marquardt algorithm. *IEEE Trans. Microw. Theory Tech.* **2019**, *67*, 1138–1147. [\[CrossRef\]](#)
44. Rekanos, I.T.; Raisanen, A. Microwave imaging in the time domain of buried multiple scatterers by using an FDTD-based optimization technique. *IEEE Trans. Magn.* **2003**, *39*, 1381–1384. [\[CrossRef\]](#)
45. Meng, Q.; Ye, D.; Huangfu, J.; Li, C.; Ran, L. Experimental investigation on through-wall imaging based on non-linear inversions. *Electron. Lett.* **2016**, *52*, 1933–1935. [\[CrossRef\]](#)
46. Song, L.-P.; Yu, C.; Liu, Q.H. Through-wall imaging (TWI) by radar: 2-D tomographic results and analyses. *IEEE Trans. Geosci. Remote Sens.* **2005**, *43*, 2793–2798. [\[CrossRef\]](#)
47. Estatico, C.; Fedeli, A.; Pastorino, M.; Randazzo, A. Quantitative microwave imaging method in Lebesgue spaces with nonconstant exponents. *IEEE Trans. Antennas Propag.* **2018**, *66*, 7282–7294. [\[CrossRef\]](#)
48. Bisio, I.; Estatico, C.; Fedeli, A.; Lavagetto, F.; Pastorino, M.; Randazzo, A.; Sciarra, A. Variable-exponent Lebesgue-space inversion for brain stroke microwave imaging. *IEEE Trans. Microw. Theory Tech.* **2020**, *68*, 1882–1895. [\[CrossRef\]](#)
49. Chew, W.C. *Waves and Fields in Inhomogeneous Media*; IEEE Press: Piscataway, NY, USA, 1995.
50. Soldovieri, F.; Brancaccio, A.; Leone, G.; Pierri, R. Shape reconstruction of perfectly conducting objects by multiview experimental data. *IEEE Trans. Geosci. Remote Sens.* **2005**, *43*, 65–71. [\[CrossRef\]](#)
51. Diening, L.; Harjulehto, P.; Hästö, P.; Ruzicka, M. *Lebesgue and Sobolev Spaces with Variable Exponents*; Lecture Notes in Mathematics; Springer: Heidelberg, Germany; New York, NY, USA, 2011; Volume 2017.
52. Estatico, C.; Fedeli, A.; Pastorino, M.; Randazzo, A. Microwave imaging by means of Lebesgue-space inversion: An overview. *Electronics* **2019**, *8*, 945. [\[CrossRef\]](#)
53. Estatico, C.; Pastorino, M.; Randazzo, A.; Tavanti, E. Three-dimensional microwave imaging in L_p Banach spaces: Numerical and experimental results. *IEEE Trans. Comput. Imaging* **2018**, *4*, 609–623. [\[CrossRef\]](#)
54. PulseEKKO, Overview, Sensors & Software. Available online: <https://www.sensoft.ca/products/pulseekko/overview-pulseekko/> (accessed on 12 April 2021).

-
55. Yoon, Y.-S.; Amin, M.G. Spatial filtering for wall-clutter mitigation in through-the-wall radar imaging. *IEEE Trans. Geosci. Remote Sens.* **2009**, *47*, 3192–3208. [[CrossRef](#)]
 56. Solimene, R.; Catapano, I.; Gennarelli, G.; Cuccaro, A.; Dell'Aversano, A.; Soldovieri, F. SAR imaging algorithms and some unconventional applications: A unified mathematical overview. *IEEE Signal Process. Mag.* **2014**, *31*, 90–98. [[CrossRef](#)]
 57. Ahmad, F.; Zhang, Y.; Amin, M.G. Three-dimensional wideband beamforming for imaging through a single wall. *IEEE Geosci. Remote Sens. Lett.* **2008**, *5*, 176–179. [[CrossRef](#)]
 58. Pisa, S.; Piuze, E.; Pittella, E.; D'Atanasio, P.; Zambotti, A.; Sacco, G. Comparison between delay and sum and range migration algorithms for image reconstruction in through-the-wall radar imaging systems. *IEEE J. Electromagn. RF Microw. Med. Biol.* **2018**, *2*, 270–276. [[CrossRef](#)]